3D image reconstruction for a Compton SPECT camera model [1]

Anne C. Sauve[2], *Student Member, IEEE*, Alfred O. Hero III[2], *Fellow, IEEE*, W. Leslie Rogers[3], *Member, IEEE*, Scott J. Wilderman[4], and Neal H. Clinthorne[3], *Member, IEEE*

[2]Dept. of Electrical Engineering and Computer Science, The University of Michigan, Ann Arbor, MI 48109-2122

[3]Dept. of Nuclear Medicine, The University of Michigan, Ann Arbor, MI 48109-0552

[4]Dept. of Nuclear Engineering and Radiologic Sciences, The University of Michigan, Ann Arbor, MI 48109-2104

Abstract

In this paper we propose a 3D image reconstruction algorithm for a 3D Compton camera being developed at the University of Michigan. We present a mathematical model of the transition matrix of the camera which exploits symmetries by using an adapted spatial sampling pattern in the object domain. For each projection angle, the sampling pattern is uniform over a set of equispaced nested hemispheres. By using this sampling pattern the system matrix is reduced to a product of a (approximately) block circulant matrix and a sparse interpolation matrix. This representation reduces the very high storage and computation requirement inherent to 3D reconstruction using transition matrix inversion methods. We geometrically optimize our hemispherical sampling and propose a 3D volumetric interpolation. Finally, we present a 3D image reconstruction method which uses the Gauss-Seidel algorithm to minimize a penalized least square objective.

I. Introduction: 3D Compton scatter SPECT camera

Application of the Compton scatter aperture to imaging in nuclear medicine was first proposed in 1974 by Todd and Everett [1]. This camera uses an innovative electronic collimator based on the Compton scattering effect. Since axial slice collimation is not used the Compton scatter camera requires a full 3D image reconstruction algorithm. Singh and Doria [2] proposed in 1983 a linear image reconstruction method for the Compton camera. This reconstruction is computationally attractive but does not take account of Doppler broadening nor the Poisson nature of the measurements. Hebert, Leahy and Singh [3] [4] implemented an MLE reconstruction from the transition matrix T that takes into account the Poisson noise for a prototype system. This algorithm is computationally demanding since even a 3D image of moderate size (128^3 pixels) requires a very large T matrix (128^6 entries).

The Compton aperture consists of a position sensitive solid state detector (det_1) with high energy resolution. This aperture is paired with a second position sensitive detector (det_2), which is a scintillation camera with lower energy resolution. The γ rays from the point source, X, that reach det_1 are Compton scattered by the solid state detector, det_1 (Fig. 1). Those scattered photons are then detected by the second detector in coincidence with the events in det_1. The energy deposited in det_1 increases as a function of the scattering angle θ according to Klein-Nishina modified to include Doppler broadening. Since the vector describing the scattered photon is known from the two detected positions in det_1 and det_2, the incident direction of the emitted photon on det_1 can be computed within a conical ambiguity. Although mechanical collimation is simple and relatively inexpensive to implement, it has the fundamental drawback of poor sensitivity. In the case of low energy parallel hole collimatosr, and without considering attenuation and scatter effects, only about 10^{-4} of the emitted photons are detected. Efforts have been made to develop electronic collimators which overcome the drawbacks of mechanical collimation. These collimators, since they utilize as many emitted photons as possible from all directions, improve the solid angle of detection and therefore provide improved detection efficiency and sensitivity over mechanical collimators [5]. The Compton scatter aperture is one such collimator.

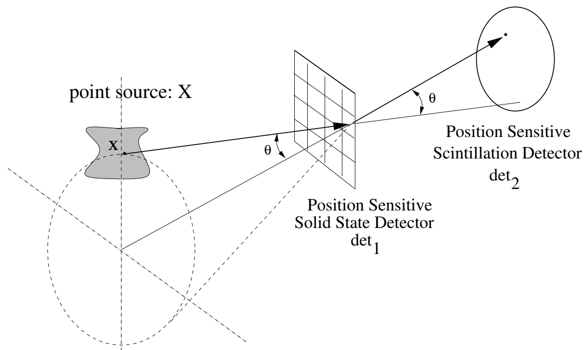

Figure 1: Conical ambiguity in the Compton Camera

In the Compton scatter collimator det_1, each resolution element can be thought of as a "pinhole" whose response function at each energy interval is an ellipse on the surface of det_2. Sensitivity gains derive from the fact that, unlike the case for a real pinhole, a resolution element in det_2 is sensitive to primary γ rays incident from many angles. Further, since the position of the scatter event in det_1 is known, the number and density of these resolution elements may be increased without introducing any ambiguity concerning the particular "pinhole" the photon passed through. This means that the sensitivity increases in approximate proportion to the solid angle subtended by det_1. The actual sensitivity increase depends on the total mass of detector 1 and the imaging geometry. Two orders of magnitude or more sensitivity increase over a collimator is possible [6]. Moreover, electronic collimation provides multiple views simultaneously. One of

[1]This work was supported by U.S. DHHS under NIH grant R01 CA32846.

the open questions has been whether it is possible to attain equivalent or better image resolution and noise properties than with mechanical collimators using fast algorithms based on sparse matrix computations and sparse system modeling. This paper presents results in this direction.

Important indices which may be helpful to the reader are:

- q = # source pixels in field of view,
- k = # detector pixels on $\det_2$,
- p = # energy levels on $\det_1$,
- M = # of rotation angles in projection set,
- l = # of radial samples in hemispheric object sampling,
- n = # of angular samples in hemispheric angles θ, ϕ, here $k = n^2$,
- N = # of Monte Carlo simulations.

II. Analytical model for system matrix

As with any statistical imaging system, the Compton camera is described by its transition probability density function relating gamma-ray emissions at source coordinates to gamma-ray detections at detector coordinates. When these coordinates are discretized into bins one obtains a transition matrix T whose entries are the transition probabilities from source bin to detector bin. It will be important to simplify the structure of T as much as possible in order to obtain computationally tractable 3D reconstructions and in order to optimize the system, e.g., through CR bound computations [7]. Here, we develop an analytical model which will reduce the memory and computation requirements for a specific (hemispherical) detector geometry. In particular, as shown below, the analytic model will reduce T to the product of sparse matrices and (approximately) circulant matrices.

Let $\{P(d_2, E, d_1|x)\}$ be the transition probabilities of the camera where:

- x: spatial location of source pixel from which gamma-ray photon is emitted
- d_1: spatial location of $\det_1$ cell where incident photon is scattered
- d_2: spatial location of $\det_2$ cell where scattered photon is recorded
- E: Compton energy detected in $\det_1$ due to scattered photon.

Let ϵ_0 be the incident energy of the emitted photon and let ϵ be the residual energy of the scattered photon. Let $\Delta\epsilon = \epsilon_0 - \epsilon$ be the Compton energy deposited into $\det_1$ due to the scattered photon. Assuming that $E = \Delta\epsilon + n$, where n is an independent energy measurement noise, that ϵ_0 is known, and that the widths ΔE of the $\det_1$ energy bins are small, the transition probability has the decomposition

$$P(d_2, E, d_1|x) = \int_0^\infty P(d_2|\epsilon, d_1, x) f(\epsilon|d_1, x) f_n(E - \epsilon) P(d_1|x) d\epsilon, \quad (1)$$

where $f_n(n) = f_n(n|d_1, x)$ is the energy measurement noise density. In what follows we will deal with each of the terms in the above factorization separately.

First we consider $P(d_2|\epsilon, d_1, x)$. For a fixed detector geometry the position d_2 on $\det_2$ where the scattered photon is detected can be specified by the two scattering angles θ and ϕ (Fig. 2). The angle θ is called the Compton scatter angle and the angle ϕ is called the out-of-plane scatter angle.

We assume the out-of-plane scatter angle ϕ to be uniformly

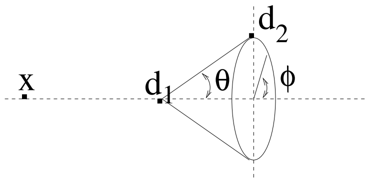

Figure 2: Definition of the angles

distributed over $[-\pi, \pi]$ independent of θ, ϵ and x. Specifically its conditional probability density is

$$f(\phi|\theta, d_1, x) = \frac{1}{2\pi}, \quad \phi \in [-\pi, \pi].$$

The conditional probability of detection of a scattered photon in cell d_2 can thus be written:

$$P(d_2|\epsilon, d_1, x) = \frac{1}{2\pi} \iint_{(\phi,\theta)\in\Omega(x,d_1,d_2)} f(\theta|\epsilon, d_1, x) d\theta d\phi, \quad (2)$$

where $f(\theta|\epsilon, d_1, x)$ denotes the conditional probability density of the Compton scatter angle θ given ϵ, d_1, x, and $\Omega(x, d_1, d_2)$ is the set of Compton and out-of-plane scatter angles such that the photon originating at x and scattered at d_1 is detected in cell at d_2.

By elementary geometrical considerations it can be seen that the scatter angle θ is specified by

$$\theta = \cos^{-1}\left(\frac{(d_1 - x)^T(d_2 - d_1)}{||d_1 - x|| \cdot ||d_2 - d_1||}\right).$$

Furthermore, when $f(\theta|\epsilon, d_1, x)$ is a smooth function of θ over $(\theta, \phi) \in \Omega(x, d_1, d_2)$ the mean value theorem can be applied to the integral (2) to obtain the approximation:

$$P(d_2|\epsilon, d_1, x) = \frac{\Delta\phi\Delta\theta}{2\pi} f(\tilde{\theta}|\epsilon, d_1, x) \approx \frac{\Delta S}{2\pi||d_1 - d_2||^2} \frac{1}{\sin\theta} f(\theta|\epsilon, d_1, x), \quad (3)$$

where $\tilde{\theta}$ is a value of θ in the range $(\theta, \phi) \in \Omega(x, d_1, d_2)$ and ΔS is the projection of the det$_2$ cell surface element at location d_2 onto the plane perpendicular to vector $d_1 - x$.

The conditional density of the scatter energy ϵ given emitter position x and detector cell d_1 is given by the **Klein-Nishina distribution** [8]:

$$f(\epsilon|d_1, x) = \frac{.572}{\epsilon_0}\left[1 + \left(2 - \frac{\epsilon_0}{\epsilon}\right)^2 + \left(1 - \frac{\epsilon_0}{\epsilon}\right)^2 \frac{\epsilon}{\epsilon_0}\right]. \quad (4)$$

From the Compton relation, the residual energy ϵ of a photon scattered off of an electron at rest are related by [8]:

$$\epsilon = \frac{\epsilon_0}{1 + \alpha(1 - \cos\theta)}, \quad (5)$$

where $\alpha = \epsilon_0/511keV$ is the ratio of incident energy to electron rest mass, and as above θ is the scatter angle. Thus in the case of an electron at rest the conditional density $f(\theta|\epsilon, d_1, x)$ is a Dirac

$$f(\theta|\epsilon, d_1, x) = \delta\left(\theta - \theta_o\right)$$

where θ_o is given by the solution of (5)

$$\theta_o = \cos^{-1}\left(1 + \frac{1}{\alpha}\left(1 - \epsilon_0/\epsilon\right)\right).$$

However, when a photon is scattered in a physical medium the angular distribution is spread out due to geometric and non-geometric effects including: depth dependent interactions, multiple scattering, and most importantly, Doppler broadening. Doppler broadening occurs due to non-zero momentum of the orbiting electron, smearing the density by as much as 10^o FWHM for low energy photons [9], [10], [11], e.g. for $\epsilon_0 = 140keV$ (Tc-99).

Fisher Von-Mises Model

The Fisher Von-Mises density $g(\xi;\beta) = \frac{\exp^{-\beta\cos\xi}}{2\pi I_o(\beta)}$, $\xi \in [-\pi, \pi]$ is analogous to the Gaussian density in that it takes the form of a bell shaped curve defined on the unit circle [12]. Here β is a shape parameter which is inversely proportional to FWHM and $I_o(\beta)$ is the modified Bessel function of the first kind of zero-th order. While a mixture model $f(\theta|\epsilon, d_1, x) = (1-\rho)g(\theta - \theta_o; \beta_1) + \rho g(\theta - \theta_o; \beta_2)$, $\rho \in (0, 1)$, might give better accuracy, especially in the area of the tails of the Doppler broadening density, for this paper we will restrict attention to the single component model $f(\theta|\epsilon, d_1, x) = g(\theta - \theta_o; \beta)$. Here, as above, $\theta_o = \arccos\left[1 + (1 - \frac{\epsilon_0}{\epsilon})/\alpha\right]$.

The density f_n of the energy measurement noise $n = E - \epsilon$ has commonly been assumed to be Gaussian [2]. However, this is a non-physical model even when the variance is of moderate magnitude since it assigns non-zero probability to negative values of E. A better model might be a non-central Chi-square distribution for E which accounts for the Gaussian distributed amplitude of the current induced at the input of a square law energy detector. Unfortunately, the use of either of these noise models requires performing the difficult integration in Eq. (1). An alternative is to refer the energy measurement noise into the θ domain via the Compton relation and (5) and use the Von Mises model to simultaneously account for geometric spreading effects, energy measurement noise, and Doppler broadening. This would ensure that negative energy measurements are assigned probability zero and, as it avoids the integration (1), yields simple closed form expressions for the transition matrix T.

Adopting the Von Mises model and combining (4), (3) and (1), we obtain

$$P(d_2, E|\epsilon, d_1, x) =$$

$$\frac{P_{1C}\Delta S\Delta E}{2\pi||d_2 - d_1||^2}\left(1 - \frac{\left((d_1 - x)^T(d_2 - d_1)\right)^2}{||d_1 - x||^2 \cdot ||d_2 - d_1||^2}\right)^{-\frac{1}{2}}$$

$$f\left(\cos^{-1}\left(\frac{(d_1 - x)^T(d_2 - d_1)}{||d_1 - x|| \cdot ||d_2 - d_1||}\right)\middle|\, \epsilon, d_1, x\right) f(\epsilon|d_1, x), \quad (6)$$

where P_{1C} is the probability of a single Compton scatter in det$_1$ (here we assume negligible photo-electric absorption).

Under the assumption that d$_2$ cell surface area is small with respect to the spread $\frac{1}{\beta}$ of the Von Mises density the representation (3) is valid and, using the identity $\cos(a + b) = \cos(a)\cos(b) - \sin(a)\sin(b)$, we obtain from (6)

$$P(d_2, E|d_1, x) \approx \frac{P_{1C}\Delta S\Delta E}{2\pi} P(E|d_1, x)$$

$$\left(1 - \frac{\left((d_1 - x)^T(d_2 - d_1)\right)^2}{||d_1 - x||^2 \cdot ||d_2 - d_1||^2}\right)^{-\frac{1}{2}} \frac{1}{2\pi I_0(\beta)||d_2 - d_1||^2}$$

$$\exp\left[-\beta\left(\frac{(d_1-x)^T(d_2-d_1)}{||d_1-x||\cdot||d_2-d_1||}\left(1 + (1 - \frac{\epsilon_0}{E})/\alpha\right)\right.\right.$$

$$\left.\left. + \sqrt{1 - \left(\frac{(d_1 - x)^T(d_1 - d_2)}{||d_1 - x|| \cdot ||d_2 - d_1||}\right)^2} \sqrt{1 - \left(1 + (1 - \frac{\epsilon_0}{E})/\alpha\right)^2}\right)\right]$$

Note that the absolute position of x has no importance: x only enters the picture through the angle between the vectors $d_1 - x$ and $d_2 - d_1$.

The above expression is rich in vector operations and is therefore suitable for fast on line computation. Note that when $d_2 - d_1$ has constant length and the det$_2$ pixel areas ΔS are constant, the probability density function $P(d_2, E|d_1, x)$ (the elements of T) have symmetries which can be exploited to reduce computation. This occurs when the detector det$_2$ is a hemisphere centered at d$_1$. Let $P(d_1|x)$ be the probability that a γ-ray emitted at x intercepts the detector surface d$_1$ (computed from the solid angle subtended by the cell d_1 from the source point x). This probability when combined with the above relation gives the required elements of the transition matrix from (1)

$$P(d_2, E, d_1|x) = P(d_2, E|d_1, x)\, P(d_1|x), \quad (7)$$

indexed over d_2, E and d$_1$.

Determination of Von-Mises Width Parameter
We here describe how we fit the Von Mises model to the density $f(\theta|\epsilon, d_1, x)$. We generated 10^9 Doppler scatter histories using the SKEPTIC photon transport simulator [13]. The simulation was performed for a $6 \times 6 \times 5$mm Germanium detector element and a $511keV$ incident photon and scattering data was collected at Compton angles ranging from 20^o to 120^o in 0.1^o increments. The simulation only accounts for angular spreading due to geometric effects and does not account for Doppler broadening or energy measurement noise. In Fig. 3.a the shifted densities of scatter angles are superimposed to illustrate the spreading variability as a function of measured energy E. The best fit Von-Mises density is shown in Fig. 3.b, where the fitting was done using the Kolmogorov procedure described below.

Several methods for estimation of β have been explored. A method using the relation [14] was implemented (for $\beta > 3$):

$$E_\beta(\cos\theta) = \int_{-\pi}^{\pi} \cos(\alpha) f_\beta(\alpha) d\alpha = \frac{I_1(\beta)}{I_0(\beta)} \approx 1 - \frac{1}{2\beta},$$

yielding the explicit estimate $\hat{\beta}_{Mom} = \frac{1}{2}\frac{1}{1-\frac{1}{N}\sum\cos\theta_i}$, where $\{\theta_i\}_{i=1}^N$ are obtained from the Monte Carlo simulation. Kolmogorov's method [15] is based on matching empirical and theoretical cumulative distribution functions:

$$\hat{\beta}_{Kd} = \underset{\beta}{argmin} \parallel F_\beta(\theta) - \hat{F}_E(\theta) \parallel_\theta^2,$$

where $F_\beta(\theta) = \int_{-\pi}^{\theta} f_\beta(\alpha) d\alpha$ is the cumulative distribution function (CDF) for the Von Mises density and $\hat{F}_E(\theta) = \int_{-\pi}^{\theta} f_E(\alpha) d\alpha$ the empirical CDF of θ obtained from Monte Carlo simulations. The Kolmogorov method gave a better fit to the data than the method of moments for our simulations.

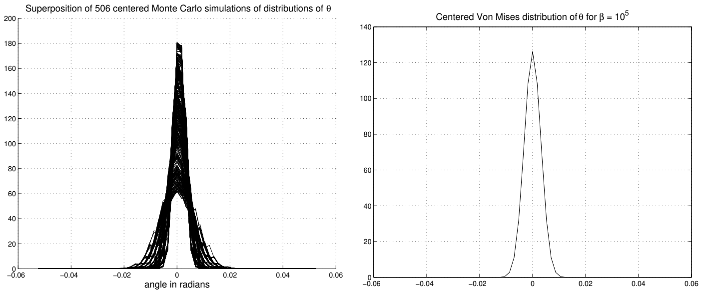

a b

Figure 3: a) Monte Carlo simulation of distribution of θ without Doppler broadening or measurement noise. Finite width of spectrum is due only to geometric spreading effects. b) Estimated Von Mises distribution of θ has parameter β on the order of 10^5.

Point source response
The forward projection on a planar detector 2 obtained for a source point is, the planar projection of a hollow cone: an annulus. Its annular width is proportional to $\frac{1}{\beta}$. In Figure 4, the forward projection is shown for a source point lying on the symmetry axis of a hemispherically shaped detector 2.

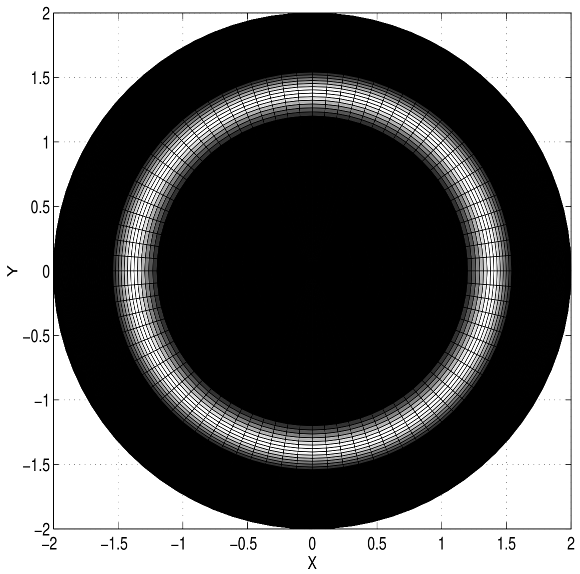

Figure 4: Forward projection obtained on detector 2 from a 511 keV source photon on the camera symmetry axis that Compton scattered on detector 1 with residual energy $E = 400$ KeV (for $\beta = 700$ and 6400 cells in detector 2).

The sinogram obtained for a source point located at the center of the field of view of the system when we rotate the detector around the Z-axis is a torus (Fig. 5). For a source point off center it can be shown that the sinogram is an undulating pipe.

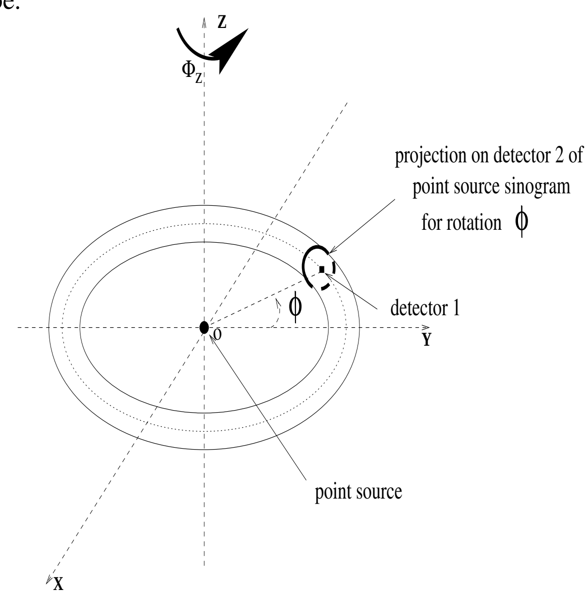

Figure 5: Torus sinogram for a point source at center of the field of view and system rotations around Z-axis

III. Camera model: Symmetry exploitation

Continuous case
It will be convenient to take $\det_2$ as a hemisphere for the purposes of symmetry exploitation. This entails no loss in

generality since any detector geometry can be rebinned into a hemisphere by reconstruction algorithm. We also restrict the discussion to the case where $\det_1$ is a unique cell at the center of the flat face of the hemisphere describing $\det_2$ (Fig. 6, Fig. 7). As we will show, this greatly reduces the storage and computation requirements due to resulting symmetries in the transition matrix.

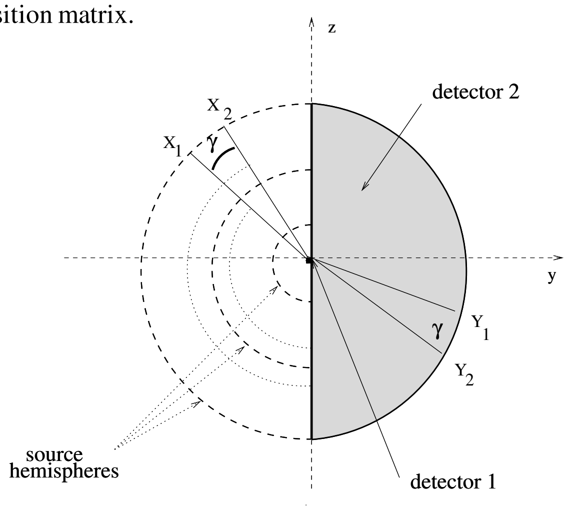

Figure 6: Source emissions leading to event trajectories $(X_1 X_2)$ and $(Y_1 Y_2)$, respectively, have identical transition probabilities.

The transition density for the continous hemispherical detector domain satisfies the following rotational symmetry property called 2D circulancy. Let X_1 and X_2 be the emission cells of two incident photons at the same distance from detector_1. Let (γ, ψ) denote the two spherical angles between $x_1 - d_1$ and $x_2 - d_1$ and assume that both photons scatter in detector_1 with the same energy E. Then the transition density functions for X_1, X_2 are simply shifted by the angles (γ, ψ). The annulus projection of the transition density function $f(d_2, E, d_1|X_2)$ is just an angularly shifted version of $f(d_2, E, d_1|X_1)$ in the variable d_2.

Discrete case

The above mentioned rotational symmetry property will only be approximate in the discretized hemisphere since there exists no uniform tesselation of the sphere that simultaneously yields equi-angular spacing and equal area pixels throughout the entire sphere. For equi-angular sampling the constant area pixel approximation error becomes worse near the polar caps of the tesselated hemisphere which can only be controlled by increasing the number of samples. Discretization methods based on spherical harmonic expansions have been recently introduced [16] which may preserve exact rotational symmetry but these will not be investigated here.

For the purposes of this paper we will use dense equi-angular sampling over $\det_2$ to induce (approximate) symmetries into the transition matrix (Fig. 7). Equi-angular sampling will allow us to simplify the 2D circulant transition matrix into a block diagonal matrix via application of the 2D FFT. By choosing the polar cap of the spherical coordinate system on axis the detector cell areas ΔS should remain approximately constant except for events at large scatter angles (high energy Compton interactions) and small angle of incidence or small scatter angles and large angles of incidence relative to the normal to $\det_1$. Thus by appropriate shielding at $\det_1$ approximate rotation invariance can be ensured if we restrict the detection to high energy interactions, which have lowest associated measurement noise. Even without shielding we anticipate that errors due to equi-angular sampling surface variations in ΔS will not be significant. This sampling produces a tesselation of the detector 2 hemisphere grid which is equivalent to a disco ball (Fig. 7).

The hemispherical geometry and the equi-angular sampled

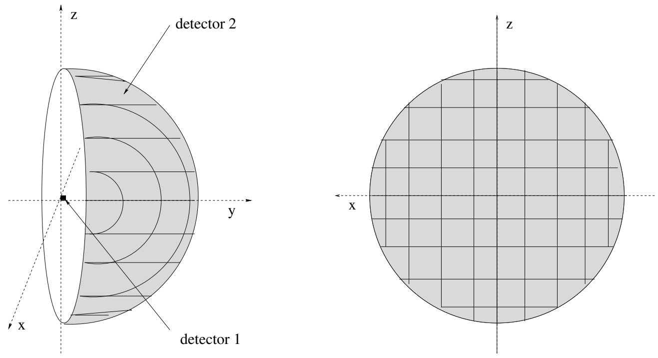

Figure 7: Nested hemispherical detector 2 with a disco ball grid

n^2 facet detector 2 induce an associated sampling in the object space. For a given orientation of detector pair $\det_1$ and $\det_2$ we use a sequence of nested hemispherical shells centered at detector 1 to sample the object space (Fig. 6 and Fig. 8). From Eq.(7) we know that two photons lying along the same ray intersecting detector 1 have identical their transition probabilities except for the solid angle factor $P(d_1|x)$. Therefore, by using such a hemispherical shells we reduce the complexity of the transition probability computations from a 3D to a 2D problem. Subsequently, we can sample each hemisphere over the same equi-angular sampling grid as detector 2 to preserve the 2D circulancy property of T.

From now on we consider the measurement equation in the discrete domain:

$$\mathbf{Y} = \mathbf{T}\,\mathbf{Q}\,\lambda + \mathbf{N}, \tag{8}$$

where $\mathbf{Y}$ is a vector containing the measured det1/det2 coincidence events at different Compton energies, $\mathbf{T}$ is a system matrix sampled in the object domain over sets of nested hemispheres, $\mathbf{Q}$ is a cartesian to hemispherical coordinate interpolation matrix, λ is the object intensity vector to be reconstructed in cartesian coordinates, and $\mathbf{N}$ accounts for possible system mismodeling errors and noise.

$\mathbf{T}$ can be represented as a concatenation of the transition matrices obtained for the p different measured Compton energies E_i, and $\mathbf{Q}$ is the concatenation of the interpolation matrices for the M different rotation angles of the detector pair $\det_1$ and $\det_2$.

$$\mathbf{T} = \begin{bmatrix} \mathbf{T}_{E_1} \\ \vdots \\ \mathbf{T}_{E_p} \end{bmatrix}, \tag{9}$$

$$\mathbf{Q} = \begin{bmatrix} \mathbf{Q}^{\Phi_1} \\ \vdots \\ \mathbf{Q}^{\Phi_M} \end{bmatrix}, \qquad (10)$$

where $\Phi_1, \ldots, \Phi_M$ denote M different angular positions of the detector pair around the object. Concatenation of the vectors $\{\mathbf{y}_{E,\Phi_i}\}_{i=1}^{M}$ into $\mathbf{y}_E^T = [\mathbf{y}_{E,\Phi_1}^T, \ldots, \mathbf{y}_{E,\Phi_M}^T]$ and $\{\mathbf{y}_{E_i}\}_{i=1}^{p}$ into $\mathbf{Y}^T = [\mathbf{y}_{E_1}^T, \ldots, \mathbf{y}_{E_p}^T]$ yields the measurement equation Eq.(8)

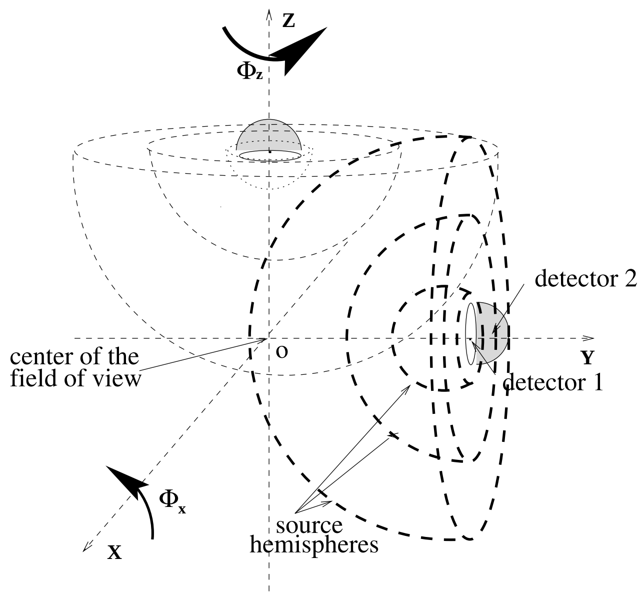

Figure 8: Hemispherical source sampling and Rotation of the detectors 1 and 2 around the field of view center

IV. Object sampling

The sequence of tesselated shells for the l different hemispheric radii form a voxelization of object space which will be used below for a given detector pair position (Fig. 8). As the detector pair is rotated about the object, the intersecting voxelization grids create an irregular sampling pattern in the object space. The sequence of M rotation angles is selected to produce a desired 3D sampling in object space. We choose a trajectory of two orthogonal orbits for the detector pair (Fig. 9) proposed by Tuy [17]. This Tuy trajectory guarantees no null-space in the system matrix T but does not guarantee that the matrix is well conditioned. We analyzed the 3D sampling in the Radon domain to assure adequate sampling for the reconstruction resolution. There is a "rule of thumb" relation [18] between detector 2 pixelization and radial resolution in the object space and between number of rotations of the detectors on the Tuy trajectory and angular resolution in the object space. To get appropriate sampling for single pixel resolution in object space for our system where $||\overrightarrow{od_1}|| = 14$ pixels, we did 30 rotations around Z-axis and 30 rotations around X-axis uniformly spread over $[0, 2\pi]$ and chose a spherical resolution $\Delta\theta \times \Delta\phi = \frac{\pi}{90} \times \frac{\pi}{90}$ on detector 2 and hemispherical source sampling shells. We sampled the field of view with 5 radii $||d_1 - x||$ from 9 to 13 pixel size.

Selected Z-slices of the corresponding sampling pattern are shown in Fig. 10. The central slice $Z = 0$ covers an area that is a disc of diameter 40 pixels. The mean number of sampling points in the cartesian voxels over the 26 Z-slices varies from 2 to 240 points per voxel.

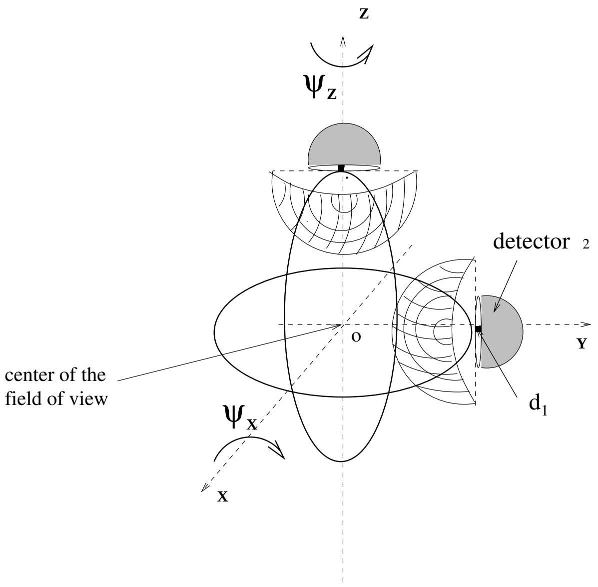

Figure 9: Two orthogonal orbits.

V. Volumetric Interpolation

Here, we discuss the interpolation method used to construct the matrix Q in Eq.(8).

A 3D interpolation from the nested hemispherical sampling pattern to the cartesian grid is necessary. It is also necessary to have very sparse interpolation matrices to be able to deal with high dimensional computations. Therefore we restricted our study to locally dependent interpolation. We developed a volumetric interpolation which induces sparseness and has low computational load. Let $\lambda(x)$ be the intensity of the object at point x. Let $C(x)$ be the cartesian voxel containing point x.

$$\lambda(x) = \frac{\sum_{x_i \in C(x)} \lambda(x_i) V_{x_i}}{\sum_{x_i \in C(x)} V_{x_i}}$$

where $\{x_i\}$ are hemispheric grid points and V_{x_i} are volumes of the polytope intersections described below. We also looked at Nearest Neighbor interpolations (NN) using pushing and pulling methods [19]. NN methods are quite sensitive to numerical 3D sampling errors since the weights are inversely proportional to intergrid distances as opposed to volumes.

Polyhedron approximation

The hemispherical voxel is defined by 4 planes and 2 spherical surfaces. The 8 vertices of this voxel are defined by two sets of 2 consecutive angles (θ_1, θ_2) and(ϕ_1, ϕ_2) and 2 consecutive radii (R_1, R_2) from the hemispherical sampling of the source. We approximated the 2 spherical surfaces by their interpolating

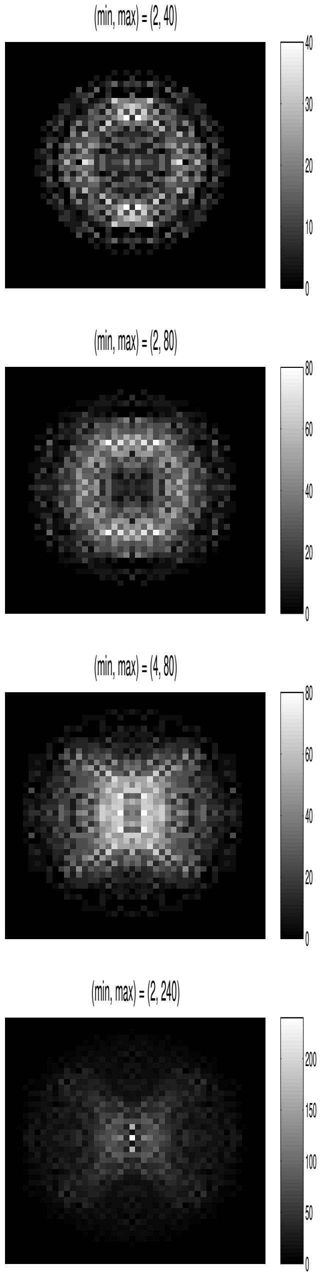

Figure 10: Slices orthogonal to the Z-axis from a pattern of 3D source sampling, for a 40x40x40 voxel image. The field of view center is at $(0, 0, 0)$. From top to bottom $Z = 12 \quad Z = 8 \quad Z = 4$ and $\quad Z = 0$.

planes to compute the intersected volumes (Fig. 11). These intersections yield a set of polyhedral volumes.

Intersections between polyhedrons and the 3D cartesian grid

Each polyhedron is defined by its 8 vertices. We call these polyhedrons hemispherical polyhedrons. We need to find the volumes V_{x_i} of all the polyhedrons generated by intersections of the 3D cartesian grid with a given hemispherical polyhedron.

In order to compute these volumes we developed a program that computes all vertices of the generated polyhedrons. First, the program picks 2 vertices from the hemispherical

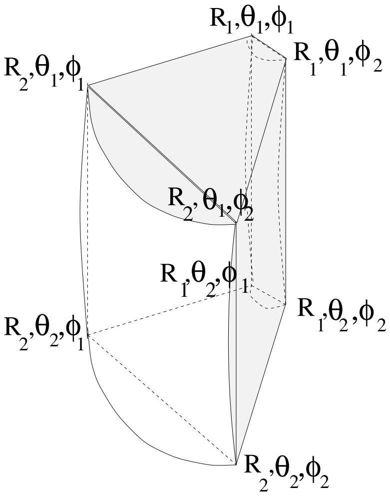

Figure 11: Approximation of hemispherical voxels by polyhedrons

polyhedron that are on an edge of the polyhedron (there are 12 such edges). Then it computes all the possible intersections between this edge and any cartesian plane. In this way we gather all the "edge" vertices of generated polyhedrons. We add to these edge vertices, the "interior" vertices that are simply the corners of the cartesian voxels inside the hemispherical polyhedron. Finally, we sort those "edge" vertices and "interior" vertices by cartesian voxel and check for redundancy and we are ready to compute the volumes of each of these generated polyhedrons (cf. Fig.12)

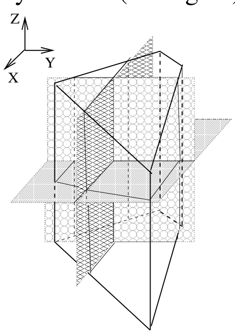

Figure 12: Intersections between one hemispherical voxel and the cartesian voxels

Volume Computation

The interpolation volumes V_{x_i} were computed using an adaptation of a very accurate LRS ANSI C program by D. Avis [20]. LRS is an implementation of the Lexicographical Reverse Search Algorithm for vertex enumeration/convex hull problems.

Given the vertices of our intersected convex polyhedron at grid point x, the LRS algorithm computes its volume, V_x. This algorithm uses the lexicographical pivot selection rule in the simplex method to return a facet enumeration of the polyhedron. From this facet enumeration, the polyhedron is then decomposed into simple non overlapping polytopes whose volumes are easy to compute.

This implementation can handle problems of quite large size, especially those composed of simple polyhedra (i.e. d-dimensional polyhedra for which the vertices are defined by only d planes). In this case, the complexity reduces to

$O(md)$ per vertex for a d-dimensional convex polyhedron defined by m inequalities. All computations are done exactly in extended precision arithmetic in any dimension [21]. These computations can all be performed off line for fixed orbit trajectory of the detector pair det_1 and det_2.

VI. Simplification of the Measurement Equation

Space domain
We can write the transition matrix $\mathbf{T}_{E_j}$ from Eq. 9 in the compact form $[(\mathbf{H}_{E_j}\mathbf{R}) \otimes \mathbf{I}_m]$ using the matrix Kronecker product notation,

$$\mathbf{H}_{E_j} = \Big(\big(\, P(d_2, E_j|d_1, x)\,\big)\Big)_{\mathbf{d_2},\mathbf{x}}, \tag{11}$$

$$\mathbf{R} = [\rho_1 \mathbf{I}_k \ldots \rho_l \mathbf{I}_k]. \tag{12}$$

where

- $k = n^2$ is the number of source pixels on one of the nested hemispheres and l is the number of hemispheres intersecting the field of view.
- I_k is the $k \times k$ identity matrix.
- $\mathbf{H}_{E_j}$ contains the transition probabilities for a given energy E_j when d_2 varies over det_2 and x varies over a single hemispheric shell in the source domain. This transition probability is constant as a function of position of detector pair and hemispherical radius $r = ||x - d_1||$. It is the only energy dependent part in $\mathbf{T}_{E_j}$.
- ρ_i is the solid angle subtended by d_1 from hemisphere i. Since ρ_i is a factor dependent only on the sampling and the geometry of the system it will be computed off-line.

Because we uniformly sample over a nested set of hemispherical grids in object space, $\mathbf{H}_{E_j}$ does not depend on the particular hemisphere. This is because, $\mathbf{H}_{E_j}$ depends on relative angles only. It is therefore 2D circulant and diagonalizable via the 2D FFT. This simplifies the transition matrix $\mathbf{T}$ as follows. Using Eqs.(8), (11) and (12) for a fixed energy E and angular position Φ, the lexicographically ordered measurements on the sampled hemispherical detector d_2 has the form:

$$\mathbf{y}_{E,\Phi} = [\mathbf{h}_E^1 \ldots \mathbf{h}_E^k]\mathbf{R}\mathbf{Q}^{\Phi}\lambda + \mathbf{n}_{E,\Phi} \tag{13}$$

2D Fourier domain
Taking the 2D Fourier transform of (13) we obtain:

$$\mathbf{W}_{n\times n}\mathbf{y}_{E,\Phi} = \tilde{\mathbf{y}}_{E,\Phi} = \tilde{\mathbf{h}}_E^{x_0} \odot (\mathbf{R}\tilde{\lambda}_{\Phi}) + \tilde{\mathbf{n}}_{E,\Phi} \tag{14}$$

where $\mathbf{W}_{n\times n}$ is the 2D FFT matrix [22, Ch. 4, p. 141], and $\tilde{\lambda}_\Phi = [\tilde{\lambda}^T_{\Phi,1}, \ldots, \tilde{\lambda}^T_{\Phi,l}]^T$ is the 2D FFT of the source intensity within each of l hemispheric shells, and $\tilde{\mathbf{h}}_E^{x_0} = \mathbf{W}_{n\times n}\mathbf{h}_E^{x_0}$ is the 2D FFT of the point response function $\big(\, P(d_2, E|d_1, x_0)\,\big)_{\mathbf{d_2}}$ for x_0 an arbitrary origin in the object space (one of the k columns of $\mathbf{H}_E$), and $\odot$ denotes the element-by-element vector product.
Note that because of the 2D circulancy of $\mathbf{H}_E$, all that remains of $\mathbf{H}_E$ in Eq.(14) is the 2D Fourier transformed transition matrix for a single source point x_0, $\tilde{\mathbf{h}}_E^{x_0}$. Transforming back to the space domain and concatenating the different angular positions of the trajectory of the detector pair:

$$\mathbf{Y_E} = \begin{bmatrix} \mathbf{W^H}_{n\times n}\left(\tilde{\mathbf{h}}_E^{x_0} \odot (\mathbf{R}\tilde{\lambda}_{\Phi_1})\right) \\ \vdots \\ \mathbf{W^H}_{n\times n}\left(\tilde{\mathbf{h}}_E^{x_0} \odot (\mathbf{R}\tilde{\lambda}_{\Phi_M})\right) \end{bmatrix} + \mathbf{N}_E \tag{15}$$

where: $\mathbf{Y_E} = \begin{bmatrix} \mathbf{y}_{E,\Phi_1} \\ \vdots \\ \mathbf{y}_{E,\Phi_m} \end{bmatrix}$, $\mathbf{N}_E = \begin{bmatrix} \mathbf{n}_{E,\Phi_1} \\ \vdots \\ \mathbf{n}_{E,\Phi_M} \end{bmatrix}$ and $\mathbf{W}^H_{n\times n}$ is the inverse 2D FFT matrix. Eq.(15) takes into account the different Compton energies. $\mathbf{Y_E}$ can be equivalently expressed as a product of matrices from which we can extract λ:

$$\mathbf{Y_E} = \mathbf{W^H}\left[\left(\mathrm{Diag}(\tilde{\mathbf{h}}_E^{x_0})\mathbf{R}\mathbf{W}\right) \otimes \mathbf{I_m}\right] \begin{bmatrix} \mathbf{Q}^{\Phi_1} \\ \vdots \\ \mathbf{Q}^{\Phi_M} \end{bmatrix} \lambda + \mathbf{N}_E, \tag{16}$$

where $\mathrm{Diag}(\tilde{\mathbf{h}}_E^{x_0})$ is a diagonal matrix which has the vector $\tilde{\mathbf{h}}_E^{x_0}$ on its main diagonal. Let us write now the measurement equation in the following compact form:

$$\mathbf{Y_E} = \mathbf{K}_E\lambda + \mathbf{N}_E.$$

Note from Eq.(12) that $\mathbf{R}$ in Eq.(16) is very sparse. This will significantly simplify the computationally demanding 3D reconstruction algorithm. Moreover, we do not have to store the very large $\mathbf{T}$ matrix but only the Fourier domain transfer function $\tilde{\mathbf{h}}_{E_j}{}^{x_0}$ and the l scalars ρ_i leading to reduction of storage requirements by several orders of magnitude.

VII. Iterative Reconstruction Algorithms

We implemented the Penalized Weighted Least Squares (PWLS) objective function:

$$\Phi(\lambda) = \sum_E (\mathbf{Y}_E - \mathbf{K}_E\lambda)^T \mathbf{V}_{Y_E}^{-1}(\mathbf{Y}_E - \mathbf{K}_E\lambda) + \alpha\lambda^T\mathbf{B}\lambda, \tag{17}$$

where the summation $\sum_E$ is over all energy bins, $\mathbf{B}$ is a non-negative definite 3D roughness penalty matrix, α is a positive scalar and $\mathbf{V}_{Y_E} = \mathrm{Cov}(\mathbf{N}_E)$. Since $\mathbf{N}_E$ is a Poisson noise $\mathrm{Cov}(\mathbf{N}_E) = \mathrm{Diag}(\mathbf{K}_E\lambda)$. We actually used $\mathbf{V}_{Y_E} = \mathrm{Diag}(\mathbf{K}_E\lambda + \epsilon)$ to insure $\mathbf{V}_{Y_E}$ is not ill-conditionned. We minimized the PWLS objective function using Gauss-Seidel (GS) algorithm which updates one pixel at a time holding the other fixed to most recent values.

Numerical Results

We implemented the PLS on a single 3D point object in the center of the field of view $40 \times 40 \times 40$ pixels without noise. We chose the smoothing parameter α very small only to counteract numerical roundoff errors. After 150 iterations of the GS algorithm we obtained the point spread function of our camera model. You can see the central Z-slices of the object, the initialization object and the point spread function in Fig. 13. For the GS algorithm to converge rapidly we initialized the iterations with a gaussian blurred object. You see some spreading over the 3 central slices in the point spread function.

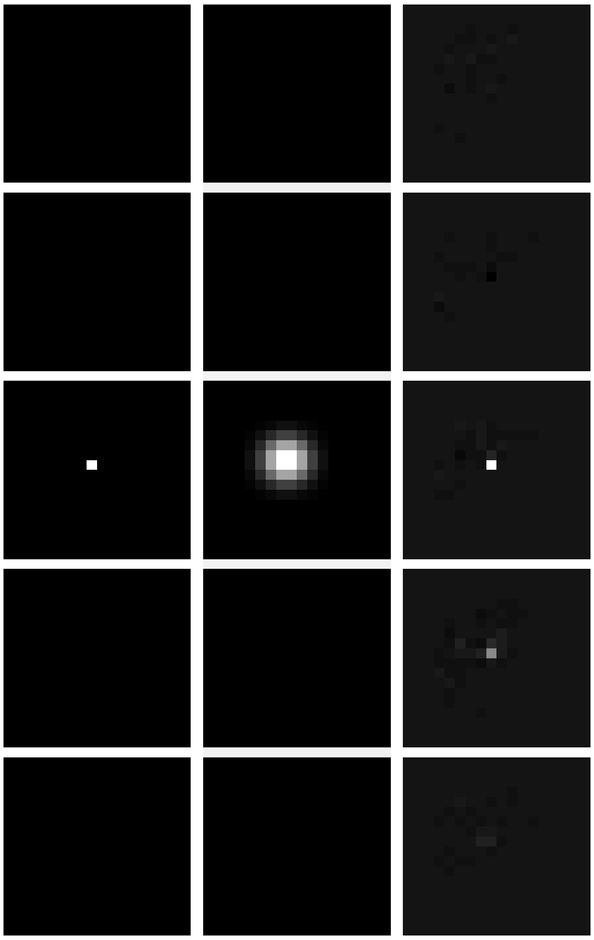

a) b) c)

Figure 13: a) original 3D object b) blurred initialization c) reconstructed 3D object with PLS in no noise case, for very small $\alpha = 10^{-18}$ and after 150 GS iterations.

VIII. Conclusion

We developed an analytical model to compute the transition matrix of a Compton camera that is rich in vector operations and is the product of block circulant and sparse matrices. To accomplish this we developed a volumetric interpolation which is robust to 3D sampling errors, optimized geometrically the source sampling pattern making it as uniform as possible in the object domain, and developed a 3D reconstruction based on Fourier domain methods. Note in this application of least squares, we have not included weighting to account for Poisson noise. In a future paper, we will present reconstruction algorithms which fully utilize Poisson statistics.

IX. Acknowledgements

The authors wish to thank the Editor and the anonymous reviewers for comments that led to an improvement in the presentation of these results. We would also like to thank David Avis for making his LRS ANSI C program available to us and Jeffrey Fessler for helpful discussions concerning the reconstruction algorithms.

X. References

[1] R. Todd, J. Nightingale, and D. Everett, “A proposed Gamma camera,” *Nature*, vol. 251, pp. 132–134, 1974.

[2] M. Singh and D. Doria, “An electronically collimated gamma camera for single photon emission computed tomography, part II: Image reconstruction and preliminary experimental measurements,” *Medical Physics*, vol. 10, no. 4, pp. 428–435, 1983.

[3] T. Hebert, R. Leahy, and M. Singh, “Maximum likelihood reconstruction for a prototype electronically collimated single photon emission system,” in *Proc. SPIE Medical Imaging*, vol. 767, pp. 77–83, 1987.

[4] T. Hebert, R. Leahy, and M. Singh, “Three-dimensional maximum-likelihood reconstruction for a electronically collimated single-photon-emission imaging system,” in *J. Opt. Soc. Am. A*, vol. 7, pp. 1305–1313, July 1990.

[5] N. H. Clinthorne, C. yi Ng, C. ho Hua, J. E. Gormley, J. W. Leblanc, S. J. Wilderman, and W. L. Rogers, “Theoretical performance comparison of a Compton-scatter aperture and parallel-hole collimator,” *Conference Record of the 1996 IEEE Nuclear Science Symposium*, 1996.

[6] J. W. Leblanc, *A Compton camera for low energy gamma ray imaging in nuclear medicine applications*. PhD thesis, UM Ann-Arbor, 1999.

[7] N. H. Clinthorne, C. Ng, C. Hua, J. E. Gormely, J. Leblanc, S. J. Wilderman, and W. L. Rogers, “Theoretical peformance comparison of a Compton-scatter aperture and parallel-hole collimator,” *Nuclear Sciences*, vol. NS-43, no. 4, 1996.

[8] G. F. Knoll, *Radiation Detection and Measurement*. Wiley, 1979.

[9] C. H. Hua, N. H. Clinthorne, S. J. Wilderman, J. W. LeBlanc, and W. L. Rogers, “Quantitative evaluation of information loss for Comptoncameras,” *Nuclear Sciences*, vol. NS-46, no. 4, 1999.

[10] C. Ordonez, A. Bolozdynya, and W. Chang, “Energy uncertainties in compton cameras,” in *Conference Record of the 1997 Nuclear Science Symposium and Medical Imaging Conference*, (Albuquerque, New Mexico), November 1997.

[11] W. Reed and P. Eisenberger, “Gamma-ray Compton profile of diamond, silicon and germanium,” *Physics Review B*, vol. 6, pp. 4598–4604, 1972.

[12] K. V. Mardia, *Statistics of Directional Data*. Academic Press, 1972.

[13] S. Wilderman, "Simulated Kilovolt Electron and Photon Transport In Condensed media (SKEPTIC)," *Ansi C code developed at University of Michigan, Dept. of Nuclear Engin and Radiological Sciences*, 1995.

[14] N. I. Fisher, T. Lewis, and B. J. J. Embleton, *Statistical Analysis of Spherical Data*. Cambridge University Press, 1987.

[15] P. J. Bickel and K. A. Doksum, *Mathematical Statistics: Basic Ideas and Selected Topics*. Holden-Day, San Francisco, 1977.

[16] D. M. Healy and D. N. Rockmore, "An FFT for the 2-sphere and applications," in *ICASSP*, vol. 3, pp. 7–10, May 1996.

[17] H. K. Tuy, "An inversion formula for cone-beam reconstruction," *SIAM Journal of Applied Mathematics*, vol. 43, pp. 546–552, 1983.

[18] D. B. Kay, W. Keyes, and W. Simon, "Radionuclide tomographic image reconstruction using Fourier transform techniques," *Nuclear Medicine*, vol. NM-15, pp. 981–986, 1974.

[19] W. H. Press, W. T. Vetterling, S. A. Teukolsky, and B. P. Flannery, *Numerical Recipes in C : The Art of Scientific Computing*. Cambridge, 1992.

[20] LRSA, "Lexicographical reverse search algorithm ansi C program written by D. Avis, McGill University." URL:http://www.cs.mcgill.ca/$\sim$avis.

[21] D. Avis, "A C implementation of the reverse search vertex enumeration algorithm." Research Report B-359, Department of Information Sciences, Tokyo Institute of Technology, 1992.

[22] R. N. Bracewell, *Two-Dimensional Imaging*. Prentice Hall, 1995.